FRONTIERS OF PHYSICS

RESEARCH ARTICLE
Volume 18 / Issue 6 / 63304 / 2023

Alloy-induced reduction and anisotropy change of lattice thermal conductivity in Ruddlesden–Popper phase halide perovskites

Huimin Mu[1], Kun Zhou[2], Fuyu Tian[2], Yansong Zhou[1], Guoqi Zhao[2], Yuhao Fu[1,†], Lijun Zhang[2,‡]

1 State Key Laboratory of Superhard Materials, International Center of Computational Method and Software,
College of Physics, Jilin University, Changchun 130012, China
2 State Key Laboratory of Integrated Optoelectronics, Key Laboratory of Automobile Materials of MOE,
International Center of Computational Method and Software, College of Materials Science and Engineering,
Jilin University, Changchun 130012, China
Corresponding authors. E-mail: †fuyuhaoy@gmail.com, ‡lijun_zhang@jlu.edu.cn

Received April 19, 2023; accepted May 19, 2023

ABSTRACT

The effective modulation of the thermal conductivity of halide perovskites is of great importance in optimizing their optoelectronic device performance. Based on first-principles lattice dynamics calculations, we found that alloying at the B and X sites can significantly modulate the thermal transport properties of 2D Ruddlesden–Popper (RP) phase halide perovskites, achieving a range of lattice thermal conductivity values from the lowest (κ_c = 0.05 W·m^{-1}·K^{-1}@Cs$_4$AgBiI$_8$) to the highest ($\kappa_{a/b}$ = 0.95 W·m^{-1}·K^{-1}@Cs$_4$NaBiCl$_4$I$_4$). Compared with the pure RP-phase halide perovskites and three-dimensional halide perovskite alloys, the two-dimensional halide perovskite introduces more phonon branches through alloying, resulting in stronger phonon branch coupling, which effectively scatters phonons and reduces thermal conductivity. Alloying can also dramatically regulate the thermal transport anisotropy of RP-phase halide perovskites, with the anisotropy ratio ranging from 1.22 to 4.13. Subsequently, analysis of the phonon transport modes in these structures revealed that the lower phonon velocity and shorter phonon lifetime were the main reasons for their low thermal conductivity. This work further reduces the lattice thermal conductivity of 2D pure RP-phase halide perovskites by alloying methods and provides a strong support for theoretical guidance by gaining insight into the interesting phonon transport phenomena in these compounds.

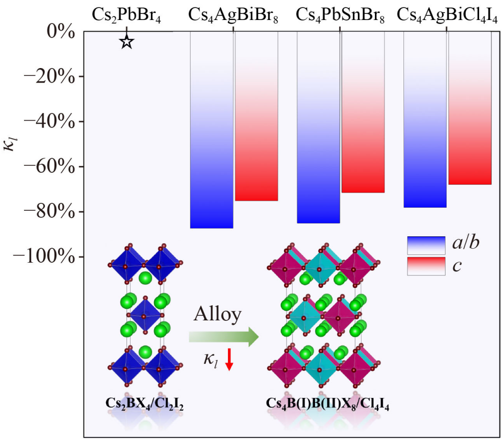

Keywords first-principles lattice dynamics calculations, Boltzmann transport, all-inorganic RP-phase halide perovskite alloys, thermal conductivity

---

Special Topic: Surface and Interface of Two-dimensional Materials (Eds.: Lijun Zhang, Dongchen Qi, Ming Yang & Kai Zhang).

Higher Education Press

https://doi.org/10.1007/s11467-023-1315-1

1 Introduction

The chemical structural formula of three-dimensional (3D) metal halide perovskite is ABX_3, where A represents a monovalent metal cation or an organic cation, B represents a divalent metal cation, and X represents a halogen anion. As a new type of semiconductor material, it has received special attention not only for its wide range of applications in fields such as piezoelectricity, ferroelectricity, and optoelectronics, but also for its potential in thermal transport [1–7]. At present, there have been many reports exploring 3D all-inorganic halide perovskites with low thermal conductivity [8–10]. This is because low lattice thermal conductivity contributes to the high thermoelectric figure of merit in most thermoelectric devices [11–16]. For instance, at 300 K, Kawano *et al.* [17] demonstrated through theoretical studies that the thermal conductivity (κ_l) of $CsSnBr_3$ is 0.84 $W\cdot m^{-1}\cdot K^{-1}$. The κ_l of Cs_2PtI_6 at 300 K to be 0.15 $W\cdot m^{-1}\cdot K^{-1}$ was calculated by Sajjad *et al.* [18]. However, numerous studies have shown that compared to 3D halide perovskites, the corresponding two-dimensional (2D) halide perovskites not only exhibit superior physical properties but also have greater stability [19–23]. For example, the stability of perovskite solar cell devices is improved by suppressing ion migration through the strong ion polarization of metal ions towards halide ions in two-dimensional perovskite materials [24]. Therefore, in the thermal management of perovskite devices, 2D halide perovskite materials may provide a more effective solution.

At present, there are relevant studies on the thermal transport behavior of 2D halide perovskite materials [25–27]. For example, Li *et al.* [28] obtained a value of 0.3 $W\cdot m^{-1}\cdot K^{-1}$ for the κ_l of 2D lead iodide perovskite crystals through theoretical calculations combined with experiments. The in-plane κ_l of Ruddlesden–Popper (RP) phase $(PEA)_2PbI_4$ to be (0.19 ± 0.03) $W\cdot m^{-1}\cdot K^{-1}$ was measured in the interlayer direction by Thakur *et al.* [27]. The in-plane κ_l of $MAPbI_3$-based RP-phase perovskite was found to be (0.37 ± 0.13) $W\cdot m^{-1}\cdot K^{-1}$, which is comparable to its 3D perovskite counterpart of κ_l [29, 30]. Recently, it is worth noting that all-inorganic RP-phase halide perovskite single crystal ($Cs_2PbI_2Cl_2$) was successfully prepared by the Bridgman method in experiments and the in-plane κ_l along the crystal *c*-axis was measured to be ~0.37–0.28 $W\cdot m^{-1}\cdot K^{-1}$ within the temperature range of 295–523 K [31]. As researchers delve deeper into the thermal transport properties of 2D halide perovskites, it has been discovered that further reducing their thermal conductivity is an important pathway to expanding their range of applications. Low thermal conductivity can improve the extraction of hot carriers and increase the conversion efficiency of photovoltaic cells, while high thermal conductivity can help to avoid thermal failure in light-emitting devices. Alloying, as one of the common means to regulate the properties of materials, provides the possibility to increase stability and reduce the thermal conductivity of materials by controlling the doping proportion and method of different elements [32–35]. For example, Slade *et al.* [36] alloyed PbSe with $NaSbSe_2$ to obtain PbSe–$NaSbSe_2$ with very low in-plane κ_l in the temperature range of 400–873 K (1–0.55 $W\cdot m^{-1}\cdot K^{-1}$). Zheng *et al.* [37] used alloying to obtain the material MgAgSb with low κ_l of 0.45 $W\cdot m^{-1}\cdot K^{-1}$ at 473 K. Therefore, a comprehensive and in-depth investigation of the effects of alloying on the thermal transport properties of 2D RP-phase halide perovskites should be conducted to promote the development and application of this field.

This work systematically investigates the thermal transport properties of all inorganic 2D RP-phase halide perovskites after alloying and the regular variation of thermal conductivity with different structural components based on first-principles lattice dynamics calculations and iterative solutions of the Boltzmann transport equation. We found that alloying at both the B and X sites can significantly modulate the thermal transport properties of 2D RP-phase halide perovskite. Compared with 2D pure RP-phase halide perovskites and 3D halide perovskite alloys, the alloying of 2D RP-phase halide perovskites introduced more phonon branches and strengthened the coupling between phonon branches, resulting in a reduction of lattice thermal conductivity. In addition, alloying can also significantly regulate the thermal transport anisotropy of RP-phase halide perovskite. Phonon transport modes of RP-phase halide perovskite alloys are also analyzed. By investigating the effect of alloying on the thermal transport of RP-phase halide perovskite materials, we hope to avoid thermal failures in perovskite devices. This study also provides new insights for designing efficient thermoelectric materials and devices.

2 Computational method

The equilibrium crystal structures and the interatomic force constants calculations (IFCs) are performed based on the density functional theory (DFT) using the projector augmented wave (PAW) method with the Vienna ab initio simulation package (VASP) [38]. We used the local density approximation (LDA) functional as the exchange-correlation functional [39]. The Hellmann–Feynman force convergence threshold is set as 1×10^{-4} $eV\cdot Å^{-1}$. The structural optimization is done with the kinetic-energy cutoff of 520 eV and Brillouin zone integration via k-point meshes of spacing $2\pi \times 0.03$ $Å^{-1}$. We explored a set of 24 halide perovskite compounds, including halide single perovskites $CsBBr_3$ (B = Ge, Sn, and Pb), double perovskites $Cs_2B(I)B(II)X_6$ (B(I) = Na and Ag; B(II) = In and Bi; X = Cl and Br), RP-phase halide perovskites Cs_2PbX_4 (X = Cl, Br, and I), $Cs_2BCl_2I_2$ (B = Sn and Pb), and RP-phase halide perovskite alloys $Cs_4B(I)B(II)X_8/Cl_4I_4$ (B(I) = Na, Ag, and Pb; B(II) = Sn and Bi; X = Cl, Br, and I). The AIMD simulations were done with 2 × 2 × 2 supercells of the single halide perovskites (with 40 atoms in total), 1 × 1 × 1 supercells of double halide perovskites (with 40 atoms in total), 2 × 2 × 1 supercells of ($n = 1$) RP-phase halide perovskites (with 56 atoms in total), and 1 × 1 × 1 supercells of RP-phase halide perovskite alloys (with 56 atoms in total). The plane-wave cutoff of 400 eV for single/double halide perovskites and 270 eV for RP-phase halide perovskites and alloys. We employed the canonical NVT ensembles at a temperature of 300 K, controlled by a Nosé–Hoover thermostat [40]. Simulations were conducted for more than 8000 timesteps of 1 fs each on single/double/RP-phase halide perovskites and for 100 000 timesteps of 1 fs each on RP-phase halide perovskite alloys to ensure the attainment of thermodynamic equilibrium.

Temperature-dependent harmonic and anharmonic interatomic force constants were calculated using a least-square method, fitting the *ab initio* molecular dynamic (AIMD) forces to a model Hamiltonian with the temperature-dependent effective potential (TDEP) method [41, 42],

$$H=U_0+\sum_i \frac{p_i^2}{2m}+\frac{1}{2}\sum_{\substack{ij\\ \alpha\beta}}\Phi_{ij}^{\alpha\beta}u_i^{\alpha}u_j^{\beta}+\frac{1}{3}\sum_{\substack{ijk\\ \alpha\beta\gamma}}\Psi_{ijk}^{\alpha\beta\gamma}u_i^{\alpha}u_j^{\beta}u_k^{\gamma}. \tag{1}$$

Here U is the potential energy, Φ and Ψ are the second- and third-order IFCs. The displacement of atom i from ideal positions is denoted $\boldsymbol{u}_i$, its momentum $\boldsymbol{p}_i$, and $\alpha\beta\gamma$ are Cartesian indices. The real-space cutoff radii are set to 5 Å for the pair and three-body interactions.

The thermal conductivity was calculated by iteratively solving the linearized phonon Boltzmann transport equation (BTE) as implemented in the ShengBTE package [43] with temperature-dependent effective harmonic and anharmonic IFCs. The κ of cubic systems can be calculated as the sum of all the phonon mode λ with branch p and wave vector q:

$$\kappa\equiv\kappa_l^{\alpha\alpha}=\frac{1}{NV}\sum_{\lambda}C_{\lambda}\upsilon_{\lambda}^{\alpha}\upsilon_{\lambda}^{\beta}\tau_{\lambda} \tag{2}$$

and

$$C_{\lambda}=\frac{\partial f_{\lambda}(\omega_{\lambda},T)}{\partial T}, \tag{3}$$

where λ denotes a phonon mode in branch p with wave vector q, N is the number of uniformly spaced q points in the Brillouin zone, V is the volume of the unit cell, C_{λ} is the heat capacity, υ_{λ} is the phonon group velocity, and the phonon lifetime τ_{λ} in relaxation time approximation is determined by the processes of two-phonon scattering from isotopic disorder ($\mathit{\Gamma}_{\lambda\lambda'}$) and three-phonon anharmonic scattering ($\mathit{\Gamma}^{\pm}_{\lambda\lambda'\lambda''}$). $1/\tau_{\lambda}$ and $\mathit{\Gamma}^{\pm}_{\lambda\lambda'\lambda''}$ can be expressed as [43–46]

$$\frac{1}{\tau_{\lambda}}=\sum_{\lambda'\lambda''}^{+}\mathit{\Gamma}^{+}_{\lambda\lambda'\lambda''}+\sum_{\lambda'\lambda''}^{-}\frac{1}{2}\mathit{\Gamma}^{-}_{\lambda\lambda'\lambda''}+\sum_{\lambda'}\mathit{\Gamma}_{\lambda\lambda'}, \tag{4}$$

$$\Gamma^{\pm}_{\lambda\lambda'\lambda''}=\frac{\hbar\pi}{8N}\begin{Bmatrix}2(f_{\lambda'}-f_{\lambda''})\\ f_{\lambda'}+f_{\lambda''}+1\end{Bmatrix}\frac{\delta(\omega_{\lambda}\pm\omega_{\lambda'}-\omega_{\lambda''})}{\omega_{\lambda}\omega_{\lambda'}\omega_{\lambda''}}\left|V^{\pm}_{\lambda\lambda'\lambda''}\right|^2, \tag{5}$$

and

$$V^{\pm}_{\lambda\lambda'\lambda''}=\sum_{i\epsilon u.c.}\sum_{j,k}\sum_{\alpha\beta\gamma}\frac{e_{\lambda}^{\alpha}(i)\,e_{p'\pm q'}^{\beta}(j)\,e_{p''-q''}^{\gamma}(k)}{\sqrt{M_iM_jM_k}}\Phi_{ijk}^{\alpha\beta\gamma}, \tag{6}$$

where the upper (lower) row in curly brackets goes with the depend on the third-order + (−) sign for absorption (emission) processes, respectively. The scattering matrix elements $V_{\lambda\lambda'\lambda''}$ interatomic force constants (IFCs). The three-phonon scattering phase space $W^{\pm}$ (harmonic phonon frequencies contributed to the anharmonic scattering) is written as

$$W^{\pm}_{\lambda}=\frac{1}{2N}\sum_{\lambda'p''}\begin{Bmatrix}2(f_{\lambda'}-f_{\lambda''})\\ f_{\lambda'}+f_{\lambda''}+1\end{Bmatrix}\frac{\delta(\omega_{\lambda}\pm\omega_{\lambda'}-\omega_{\lambda''})}{\omega_{\lambda}\omega_{\lambda'}\omega_{\lambda''}}. \tag{7}$$

In addition, the Q-grid mesh with 15 × 15 × 15 of the single halide perovskites, 7 × 7 × 7 of double halide perovskites, 12 × 12 × 4 of ($n = 1$) RP-phase halide perovskites, and 6 × 6 × 4 of ($n = 1$) RP-phase halide perovskite alloys are chosen for obtaining the converged κ_l.

3 Results and discussion

3.1 Structure and thermal conductivity

The optimized halide perovskite alloys $Cs_4B(I)B(II)X_8/Cl_4I_4$ (B(I) = Na, Ag, and Pb; B(II) = Sn and Bi; X = Cl, Br, and I) are 2D RP-phase structures with $n = 1$, belong to the I4/mmm space group, as shown in Fig. 1(a). The 2D $B(I)/B(II)X_6$ plane is composed of octahedral structural units centered on B(I)/B(II) metal atoms, where X halogen ions occupy both internal and external positions in the plane as shared vertices of the B(I)/B(II) octahedra, with Cs^+ separating the octahedral structural units. During the optimization process, the ion positions, cell volume, and cell shape were fully relaxed. The resulting equilibrium lattice parameters were in good agreement with the experimental data, as summarized in Table S1 of the Electronic Supplementary Materials (ESM). The lattice constants follow the order of $Cs_4B(I)$

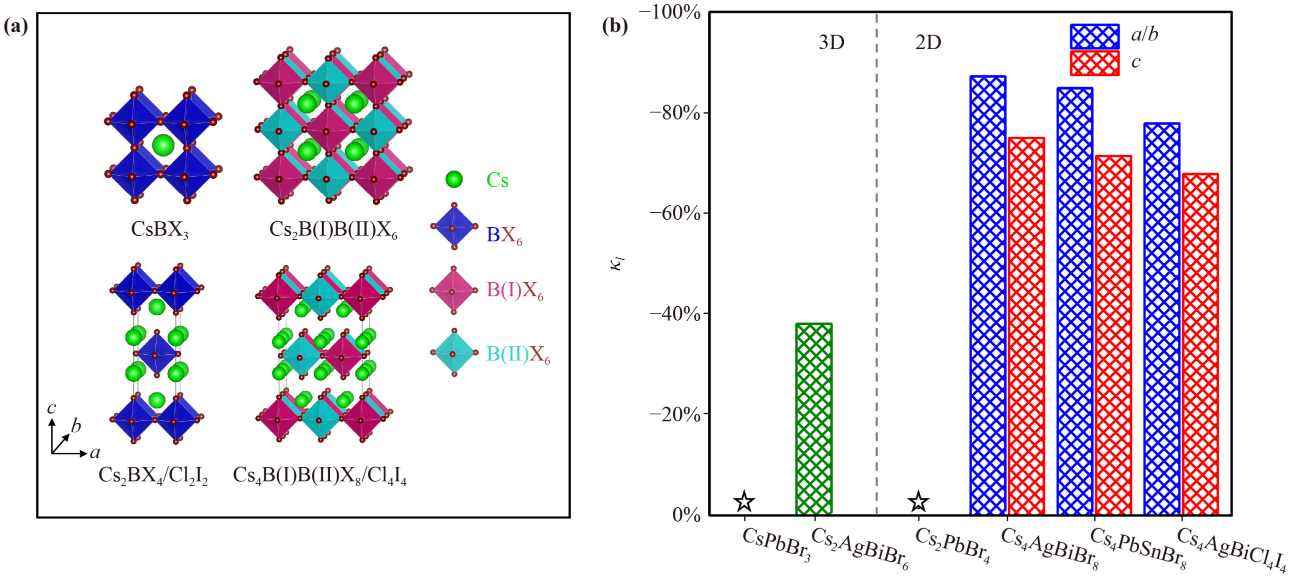

Fig. 1 **(a)** Schematic representation of the crystal structure of halide single perovskite (CsBX$_3$), double perovskite (Cs$_2$B(I) B(II)X$_6$), RP-phase halide perovskite (Cs$_2$BX$_4$/Cl$_2$I$_2$) and RP-phase halide perovskite alloy (Cs$_4$B(I)B(II)X$_8$/Cl$_4$I$_4$). **(b)** The relative percentage differences of thermal conductivity calculated at 300 K with CsPbBr$_3$ as reference for Cs$_2$AgBiBr$_6$, and with Cs$_2$PbBr$_4$ as reference for Cs$_4$AgBiBr$_8$, Cs$_4$PbSnBr$_8$ and Cs$_4$AgBiCl$_4$I$_4$.

B(II)Cl$_8$ < Cs$_4$B(I)B(II)Br$_8$ < Cs$_4$B(I)B(II)I$_8$, which is due to the increase in bond length between the metal ion at the center of the octahedron and the halogen ion as the halogen ion radius (Cl@181 pm < Br@196 pm < I@220 pm [47]) increases. The calculation of decomposition enthalpy provides guidance and reference for the synthesis process of compounds in experiments [48–50]. Therefore, we analyzed the thermodynamic stability of all inorganic RP-phase halide perovskite alloys by calculating the decomposition enthalpy, as shown in Fig. S1 of the ESM. The results showed that the decomposition enthalpies of all structures were ≤ 0, indicating that they are thermodynamically stable. We found that the Cs$_4$PbSnCl$_8$ compound had the lowest decomposition enthalpy, making it easier to synthesize experimentally.

Based on the temperature-dependent 2nd and 3rd order force constants, the lattice thermal conductivity of halide single perovskites CsBBr$_3$ (B = Ge, Sn, and Pb), double perovskites Cs$_2$B(I)B(II)X$_6$ (B(I) = Na and Ag; B(II) = In and Bi; X = Cl and Br), RP-phase halide perovskites Cs$_2$PbX$_4$ (X = Cl, Br, and I), Cs$_2$BCl$_2$I$_2$ (B = Sn and Pb), and RP-phase halide perovskite alloys Cs$_4$B(I)B(II)X$_8$/Cl$_4$I$_4$ (B(I) = Na, Ag, and Pb; B(II) = Sn and Bi; X = Cl, Br, and I) at 300 K were calculated by solving the Boltzmann transport equation. The specific values are provided in Table S1 of the ESM. Our computational results indicate that these compounds have low κ_l. At 300 K, the κ_l along the c-axis of alloyed halide perovskites even lower than that of the well-known thermoelectric material (e.g., AgSbSe$_2$@0.48 W·m^{-1}·K^{-1} and Bi$_2$Te$_3$@1.24 W·m^{-1}·K^{-1}) [42, 43]. We further analyzed the relative magnitude changes in thermal conductivity of the 3D and 2D alloy structures, using CsPbI$_3$ and Cs$_2$PbBr$_4$ as reference materials, respectively. Figure 1(b) shows the relative percentage differences of the caculated thermal conductivity with CsPbBr$_3$ as reference for Cs$_2$AgBiBr$_6$, and with Cs$_2$PbBr$_4$ as reference for Cs$_4$AgBiBr$_8$, Cs$_4$PbSnBr$_8$ and Cs$_4$AgBiCl$_4$I$_4$ at 300 K. As shown in Fig. 1(b), the thermal conductivity of Cs$_2$AgBiBr$_6$ was observed to decrease by approximately 40.0% after alloying the B site with CsPbBr$_3$. This indicates that thermal conductivity in 3D halide perovskites can be regulated through alloying. Similarly, after alloying the B site of the 2D pure RP-phase Cs$_2$PbBr$_4$, the thermal conductivity of Cs$_4$AgBiBr$_8$ decreased by 87.2% and 75.0% along the a/b and c axes, respectively. The thermal conductivity of Cs$_4$PbSnBr$_8$ obtained after alloying is 84.9% and 71.4% along the a/b and c axes, respectively. The results show a significant reduction in the thermal conductivity of 2D halide perovskites after alloying. It is noted that heterovalent alloying has a more pronounced effect on reducing the thermal conductivity of the structure than isovalent alloying. In addition, the thermal conductivity of the Cs$_4$AgBiCl$_4$I$_4$ reduced by 77.9% and 67.9% along the a/b and c axes, respectively. Therefore, in 2D halide perovskites, alloying the B site cations is more effective in reducing thermal conductivity than alloying the X site anions. The above results demonstrate that alloying method is extremely effective in reducing the thermal conductivity of 2D halide perovskites.

3.2 Phonon dispersion and density of states

We next investigated the phonon transport properties of

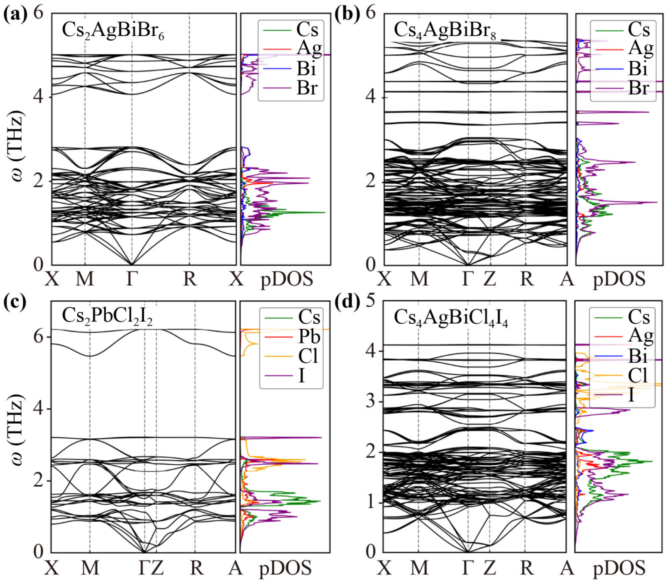

Fig. 2 Phonon dispersions along the high-symmetry k-points in irreducible Brillouin zone and the corresponding partial density of states (pDOS) of **(a)** $\mathrm{Cs_2AgBiBr_6}$, **(b)** $\mathrm{Cs_4AgBiBr_8}$, **(c)** $\mathrm{Cs_2PbCl_2I_2}$, and **(d)** $\mathrm{Cs_4AgBiCl_4I_4}$.

representative RP-phase halide perovskite alloys $\mathrm{Cs_4AgBiBr_8}$ and $\mathrm{Cs_4AgBiCl_4I_4}$. In order to highlight the effectiveness of our alloying strategy, we also compared the phonon properties of the aforementioned two structures with the extensively studied 3D double halide perovskite $\mathrm{Cs_2AgBiBr_6}$ and the 2D pure RP-phase halide perovskite $\mathrm{Cs_2PbCl_2I_2}$. The phonon dispersion of these structures was obtained by diagonalizing the temperature-dependent second-order force constants. The calculated phonon dispersions and corresponding partial density of states are shown in Fig. 2. The absence of imaginary phonon frequencies in the phonon dispersion indicates the dynamical stability of these structured compounds. The phonon dispersion of other structures is provided in Fig. S2 of the ESM. All the RP-phase halide perovskite alloys studied in our work have 56 atoms in their primitive cells, resulting in a total of 168 phonon branches in the unit cell, including three acoustic phonon branches and 165 optical phonon branches. As shown in Figs. 2(a) and (b), $\mathrm{Cs_4AgBiBr_8}$ and $\mathrm{Cs_4AgBiCl_4I_4}$ exhibit very similar dispersion curves along high-symmetry paths in the entire Brillouin zone. Interestingly, compared to the 3D $\mathrm{Cs_2AgBiBr_6}$, the frequency of the acoustic phonon branch in the RP-phase $\mathrm{Cs_4AgBiBr_8}$ is significantly lowered, resulting in a reduced phonon velocity. Additionally, compared to $\mathrm{Cs_2AgBiBr_6}$, $\mathrm{Cs_4AgBiBr_8}$ exhibits a more pronounced crossing between the optical and acoustic phonon branches in the low-frequency region ($<$ 1 THz). The strong coupling between the optical and acoustic phonon branches in $\mathrm{Cs_4AgBiBr_8}$ can lead to more phonon scattering, and alloying introduces more flat optical phonon branches with almost zero phonon velocity, both of which contribute to the lower value of κ_l in $\mathrm{Cs_4AgBiBr_8}$. Furthermore, the phonon dispersions of $\mathrm{Cs_2AgBiBr_6}$ and $\mathrm{Cs_4AgBiBr_8}$ in the low-frequency region are mainly contributed by the vibrations of Cs and Br atoms. In the case of the RP-phase $\mathrm{Cs_2PbCl_2I_2}$, the phonon branches in the low-frequency region ($<$ 1.5 THz) are mainly contributed by the vibrations of Cs, Pb, and I atoms, as shown in Fig. 2(c). As shown in Fig. 2(d), the phonon dispersion of $\mathrm{Cs_4AgBiCl_4I_4}$ is mainly contributed by the vibrations of Cs, Bi, and I atoms in the low-frequency region ($<$ 1.5 THz). Similarly, more phonon branches are also introduced after the B site alloying of pure phase $\mathrm{Cs_2PbCl_2I_2}$, resulting in stronger phonon-phonon coupling. In addition, in the structural system of $\mathrm{Cs_4B(I)B(II)X_8}$ (B(I) = Na, Ag, and Pb; B(II) = Bi; X = Cl, Br, and I), the mass of the unit cell increases with an increasing atomic mass of the X site halogen atoms (e.g., $\mathrm{Cs_4AgBiCl_8}$@1132.10 a.u. $<$ $\mathrm{Cs_4AgBiBr_8}$@1487.70 a.u. $<$ $\mathrm{Cs_4AgBiI_8}$@1863.70 a.u.). As a result, the acoustic frequency range gradually decreases, and the phonon branches soften, as shown in Fig. S2 of the ESM.

3.3 Phonon transport properties

To further understand the underlying mechanism of the phonon contributions to thermal conductivity in different frequency ranges, we calculated the normalized cumulative thermal conductivity (κ_l) and thermal conductivity spectra (κ_ω) at 300 K. The results indicate that the normalized cumulative κ_l in the a/b and c directions of the 2D RP-phase halide perovskite alloy $\mathrm{Cs_4AgBiBr_8}$ are mainly contributed by phonon modes with frequencies $<$ 3 THz and $<$ 2 THz, respectively, and reach their maximum values at 2 THz and 4 THz, respectively. On the other hand, in $\mathrm{Cs_2AgBiBr_6}$, the normalized cumulative κ_l is mainly contributed by phonon modes with frequencies $<$ 3 THz and reaches its maximum value at 5 THz. Therefore, alloying leads to a faster accumulation of the normalized cumulative κ_l in $\mathrm{Cs_4AgBiBr_8}$ compared to $\mathrm{Cs_2AgBiBr_6}$, as shown in Figs. 3(a) and (b). It is noteworthy that although the phonon branch range contributes to the normalized cumulative κ_l in $\mathrm{Cs_4AgBiBr_8}$ is comparable to that of $\mathrm{Cs_2AgBiBr_6}$, the peak is lower. In addition, the phonon branch at intermediate frequencies (4–6 THz) in $\mathrm{Cs_4AgBiBr_8}$ contributes negligibly to κ_l, resulting in a lower κ_l in $\mathrm{Cs_4AgBiBr_8}$. After reducing the dimensions and introducing alloying into $\mathrm{Cs_2AgBiBr_6}$, the number of atoms in the $\mathrm{Cs_4AgBiBr_8}$ unit cell increased. As a result, the low-frequency phonon branches showed an increase, and there was a strengthening of the phonon–phonon coupling, as illustrated in Figs. 2(a) and (b). As a result of the reduction in the frequency range of phonons that $\mathrm{Cs_4AgBiBr_8}$ contributes to thermal conductivity. The interlayer direction of $\mathrm{Cs_4AgBiBr_8}$ is oriented along the c-axis, which exhibits weaker chemical

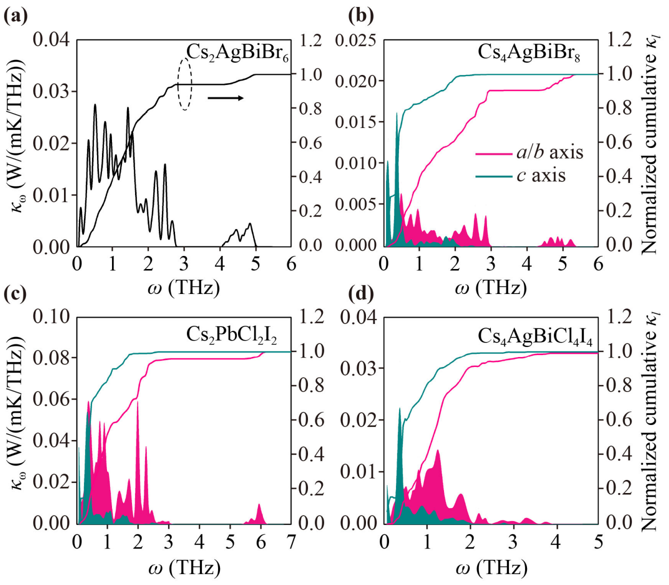

Fig. 3 Spectral (κ_ω) and normalized cumulative thermal conductivity (κ_l) of **(a)** Cs$_2$AgBiBr$_6$, **(b)** Cs$_4$AgBiBr$_8$, **(c)** Cs$_2$PbCl$_2$I$_2$, and **(d)** Cs$_4$AgBiCl$_4$I$_4$.

bonding compared to the a/b-axis. This results in a significant decrease in the frequency range of phonon contribution to thermal conductivity in the c-axis.

As shown in Fig. 3(c), the normalized cumulative κ_l in the a/b and c directions of the RP-phase Cs$_2$PbCl$_2$I$_2$ are mainly governed by phonon modes with frequencies < 3 THz and < 2 THz, respectively. When we replace Pb with Ag and Bi atoms, the κ_l along a/b and c aixs of Cs$_4$AgBiCl$_4$I$_4$ are mainly contributed by phonon modes with frequencies < 2 THz, and κ_l accumulates to the maximum value faster than in Cs$_2$PbCl$_2$I$_2$, as shown in Fig. 3(d). The atomic radius follows the order of Pb@119 pm > Ag@115 pm > Bi@103 pm, where the weaker Pb–X bond leads to a softening of phonon frequencies. Consequently, the frequency range of phonons that contribute to thermal conductivity in Cs$_2$PbCl$_2$I$_2$ is expected to be smaller than that in Cs$_4$AgBiCl$_4$I$_4$. However, the increase in the number of atoms in the Cs$_4$AgBiCl$_4$I$_4$ unit cell after alloying significantly increased the number of phonon branches in the 2–3 THz frequency range, as shown in Fig. 2(d). This led to a strengthening of phonon coupling, which is the main reason for the smaller frequency range of phonon contribution to thermal conductivity. After alloying the Pb atom in Cs$_2$PbCl$_2$I$_2$, the Ag and Bi atoms in Cs$_4$AgBiCl$_4$I$_4$ mainly contribute to the phonon branches with frequencies in the range of 1–2 THz, and the phonon hybridization between different branches is stronger, leading to less contribution to the thermal conductivity. Moreover, compared with the 3D double halide perovskite Cs$_2$AgBiBr$_6$, alloying evidently introduces more phonon branches, which is conducive to reducing κ_l, as shown in Fig. 2(d). The above results demonstrate that alloying has a significant promoting effect on reducing κ_l. The lattice thermal conductivity is strongly influenced by the three-phonon scattering process, which is determined by two factors: the scattering phase space (WP3) and the non-harmonicity of the structure. WP3 quantifies the number of scattering channels, which is entirely determined by the phonon dispersion of the material. Therefore, we conducted a comparative analysis of the WP3 of Cs$_2$AgBiBr$_6$, Cs$_4$AgBiBr$_8$, Cs$_2$PbCl$_2$I$_2$, and Cs$_4$AgBiCl$_4$I$_4$, as shown in Fig. S3 of the ESM. The results show that the alloyed Cs$_4$AgBiBr$_8$ and Cs$_4$AgBiCl$_4$I$_4$ have more scattering channels than Cs$_2$AgBiBr$_6$ and Cs$_2$PbCl$_2$I$_2$ after alloying, leading to lower κ_l.

Figure 4(a) shows that the anisotropy ratio of $\kappa_{a/b}/\kappa_c$ as a function of κ_a. We found that the anisotropy of thermal transport in RP-phase halide perovskites can be effectively controlled through alloying, resulting in anisotropy ratios ranging from 1.22 to 4.13. The maximum and minimum anisotropy ratios of RP phase halide perovskite alloys Cs$_4$PbSnI$_8$ and Cs$_4$NaBiCl$_4$I$_4$ are 1.22 and 4.13, respectively. Next, based on Eq. (2), we explored physical factors that may affect the κ_l of Cs$_4$B(I)B(II)X$_8$/Cl$_4$I$_4$ (B(I) = Na, Ag, and Pb; B(II) = Sn and Bi; X = Cl, Br, and I) include heat capacity (C_V), phonon velocity (v), and phonon lifetime (τ). They fundamentally determine the intrinsic κ_l of the crystal. The heat capacity, average phonon velocity, and phonon lifetime are shown in Figs. 4(b) and (d), with the calculated specific values listed in Table S2 of the ESM. The calculated results show that the C_V for these compounds are all around 1.0×10^6 J·m^{-3}·K^{-1}, and the variation range of these values exhibits small differences with different structures and compositions of the compounds. Thus, C_V is not the main factor causing differences in the thermal conductivity of these compounds. In addition, the average τ is significantly lower than those of other low κ_l perovskite materials, such as CH$_3$NH$_3$PbI$_3$ (1–20 ps), CsPbI$_3$ (1–40 ps), Cs$_2$PbCl$_2$I$_2$ (0.5–4.0 ps) [17, 31, 51]. These results indicate that the physical origin of the low κ_l of RP-phase perovskite alloys is mainly due to the lower v and shorter τ. It is noteworthy that, as shown in Fig. 4(b), for Cs$_4$AgBiX$_8$ (X = Cl, Br, and I), the C_V gradually decreases with an increasing atomic mass of the halogen at the X site (Cs$_4$AgBiCl$_8$@1.24×10^6 J·m^{-3}·K^{-1} > Cs$_4$AgBiBr$_8$@1.10×10^6 J·m^{-3}·K^{-1} > Cs$_4$AgBiI$_8$@0.91×10^6 J·m^{-3}·K^{-1}). Similarly, the v along the a/b-axis direction ($v_{a/b}$) also decreases gradually (Cs$_4$AgBiCl$_8$@206.82 m/s > Cs$_4$AgBiBr$_8$@197.06 m/s > Cs$_4$AgBiI$_8$@176.41 m/s). Although τ can effectively determine thermal transport, no clear trend was observed (Cs$_4$AgBiCl$_8$@1.82 ps, Cs$_4$AgBiBr$_8$@1.19 ps, Cs$_4$AgBiI$_8$@1.35 ps). This reveals that the regular changes in κ_l in the Cs$_4$AgBiX$_8$ (X = Cl, Br, and I) system are not dominated by τ, but by v and C_V. Similarly, in the Cs$_4$NaBiX$_8$ and Cs$_4$PbSnX$_8$ (X = Cl, Br, and I) structural systems, as

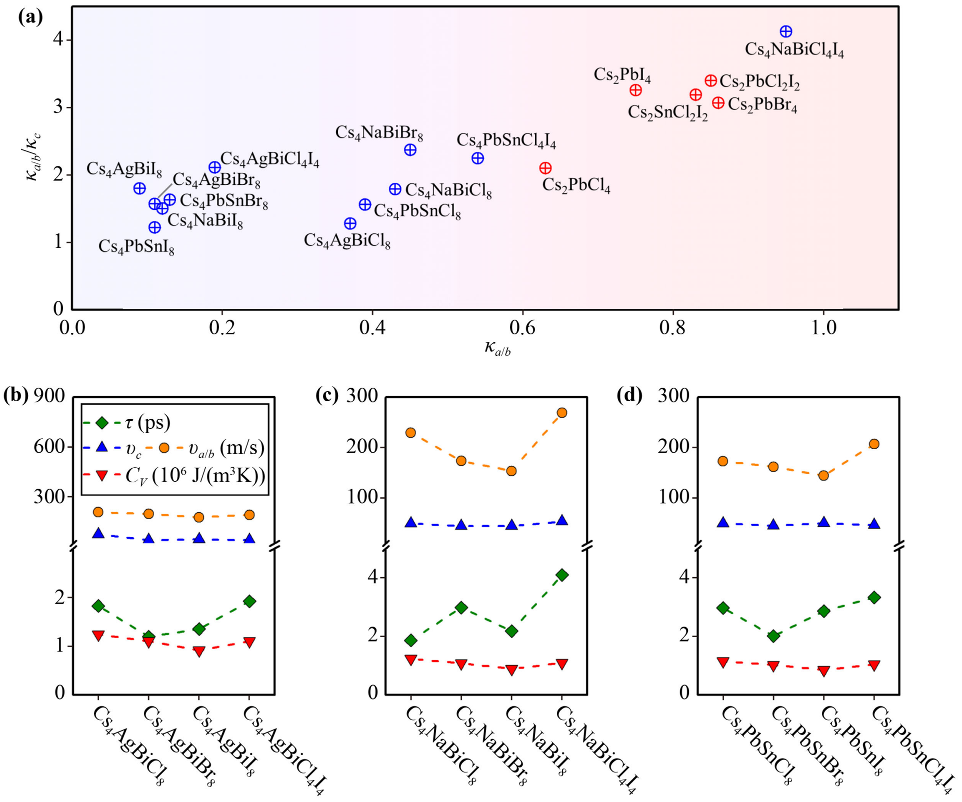

Fig. 4 **(a)** Anisotropy ratio of $\kappa_{a/b}/\kappa_c$ as a function of $\kappa_{a/b}$. **(b–d)** average phonon lifetime (τ), average phonon group velocity along the a/b ($\upsilon_{a/b}$) and c-axis (υ_c) direction and heat capacity (C_V) at 300 K of Cs$_4$B(I)B(II)X$_8$/Cl$_4$I$_4$ (B(I) = Na, Ag, and Pb; B(II) = Sn and Bi; X = Cl, Br, and I).

the mass of the halogen atoms increases, C_V and the $\upsilon_{a/b}$ decrease, while the τ still does not show any regularity, as shown in Figs. 4(c) and (d). We also observed that the $\upsilon_{a/b}$ of all the studied structures is higher than that along the c-axis, which further supports our discussion in structure and κ_l that the chemical bonds in halide perovskites are stronger along the a/b-axis. In summary, our study reveals that substituting halogen atoms in the structure can significantly adjust the average τ and the magnitude of the υ along the a/b-axis, thus effectively regulating the κ_l. In addition, we selected Cs$_4$AgBiBr$_8$ as a representative RP-phase perovskite alloy to investigate the influence of the temperature on the thermal transport properties. Our results demonstrate a gradual decrease in thermal conductivity as temperature increases. Further analysis revealed that the main cause of this decrease is a reduction in phonon lifetime, which is illustrated in Fig. S4 of the ESM.

4 Conclusions

This work systematically investigates the thermal transport properties of alloyed RP-phase halide perovskites Cs$_4$B(I)B(II)X$_8$/Cl$_4$I$_4$ (B(I) = Na, Ag, and Pb; B(II) = Sn and Bi; X = Cl, Br, and I) using first-principles lattice dynamics calculations combined with the Boltzmann transport theory. The thermal transport properties of 2D RP-phase halide perovskites can be modulated by alloying at the B and X sites in a wide range. By alloying, more strongly coupled phonon branches can be introduced into 2D RP-phase halide perovskite, which effectively scatters phonons and significantly reduces lattice thermal conductivity. The thermal transport anisotropy of RP-phase halide perovskites can be effectively regulated by alloying, with the anisotropy ratio ranging from 1.22 to 4.13. The phonon transport modes revealed that the lower phonon velocity and shorter phonon lifetime were the main reasons for low thermal conductivity of RP-phase halide perovskites. This work provides an in-depth investigation of the interesting phonon transport phenomena in RP-phase halide perovskite alloys within the framework of the Boltzmann transport theory, and offers theoretical guidance for alloy design to further reduce the thermal conductivity of materials.

Declarations The authors declare that they have no competing interests and there are no conflicts.

Availability of data and material The data that support the findings of this study are available from the corresponding author, upon reasonable request.

Electronic supplementary materials The online version contains supplementary material available at https://doi.org/10.1007/s11467-023-1315-1 and https://journal.hep.com.cn/fop/EN/10.1007/s11467-023-1315-1, including: optimized structure parameters; thermal conductivity; decomposition enthalpy; phonon dispersions and the corresponding partial density of states; scattering phase space; average phonon lifetime, average phonon group velocity and heat capacity.

Acknowledgements This work was supported by the National Key Research and Development Program of China (Grant No. 2022YFA1402501), the National Natural Science Foundation of China (Grant Nos. 12004131, 62125402, 22090044, and 92061113), and Jilin Province Science and Technology Development Program (Grant No. 20210508044RQ). Calculations were performed in part at the high-performance computing center of Jilin University.

References

1. H. Park, C. Ha, and J. H. Lee, Advances in piezoelectric halide perovskites for energy harvesting applications, *J. Mater. Chem. A* 8(46), 24353 (2020)
2. L. Zhang, J. Jiang, C. Multunas, C. Ming, Z. Chen, Y. Hu, Z. Lu, S. Pendse, R. Jia, M. Chandra, Y. Sun, T. Lu, Y. Ping, R. Sundararaman, and J. Shi, Room-temperature electrically switchable spin–valley coupling in a van Der Waals ferroelectric halide perovskite with persistent spin helix, *Nat. Photonics* 16(7), 529 (2022)
3. D. Zhang, Q. Zhang, Y. Zhu, S. Poddar, Y. Zhang, L. Gu, H. Zeng, and Z. Fan, Metal halide perovskite nanowires: Synthesis, integration, properties, and applications in optoelectronics, *Adv. Energy Mater.* 2022, 2201735 (2022)
4. T. Haeger, R. Heiderhoff, and T. Riedl, Thermal properties of metal-halide perovskites, *J. Mater. Chem. C* 8(41), 14289 (2020)
5. Y. Li, G. Na, S. Luo, X. He, and L. Zhang, Structural, thermodynamical and electronic properties of all-inorganic lead halide perovskites, *Acta Phys. -Chim. Sin.* 37(4), 2007015 (2020)
6. W. Feng, R. Zhao, X. Wang, B. Xing, Y. Zhang, X. He, and L. Zhang, Global instability index as a crystallographic stability descriptor of halide and chalcogenide perovskites, *J. Energy Chem.* 70, 1 (2022)
7. N. Jiang, B. Xing, Y. Wang, H. Zhang, D. Yin, Y. Liu, Y. Bi, L. Zhang, J. Feng, and H. Sun, Mechanically and operationally stable flexible inverted perovskite solar cells with 20.32% efficiency by a simple oligomer cross-linking method, *Sci. Bull. (Beijing)* 67(8), 794 (2022)
8. W. Lee, H. Li, A. B. Wong, D. Zhang, M. Lai, Y. Yu, Q. Kong, E. Lin, J. J. Urban, J. C. Grossman, and P. Yang, Ultralow thermal conductivity in all-inorganic halide perovskites, *Proc. Natl. Acad. Sci. USA* 114(33), 8693 (2017)
9. E. Haque and M. A. Hossain, Electronic, phonon transport and thermoelectric properties of $Cs_2InAgCl_6$ from first-principles study, *Comput. Condens. Matter* 19, e00374 (2019)
10. M. Fallah and H. M. Moghaddam, Ultra-low lattice thermal conductivity and high thermoelectric efficiency in Cs_2SnX_6 (X=Br, I): A DFT study, *Mater. Sci. Semicond. Process.* 133, 105984 (2021)
11. Y. Cai, M. Faizan, X. Shen, A. M. Mebed, T. A. Alrebdi, and X. He, NaBeAs and NaBeSb: Novel ternary pnictides with enhanced thermoelectric performance, *J. Phys. Chem. C* 127(4), 1733 (2023)
12. F. Qian, M. Hu, J. Gong, C. Ge, Y. Zhou, J. Guo, M. Chen, Z. Ge, N. P. Padture, Y. Zhou, and J. Feng, Enhanced thermoelectric performance in lead-free inorganic $CsSn_{1-x}Ge_xI_3$ perovskite semiconductors, *J. Phys. Chem. C* 124(22), 11749 (2020)
13. Q. Mahmood, M. Hassan, N. Yousaf, A. A. AlObaid, T. I. Al-Muhimeed, M. Morsi, H. Albalawi, and O. A. Alamri, Study of lead-free double perovskites halides Cs_2TiCl_6, and Cs_2TiBr_6 for optoelectronics, and thermoelectric applications, *Mater. Sci. Semicond. Process.* 137, 106180 (2022)
14. Y. X. Chen, W. Qin, A. Mansoor, A. Abbas, F. Li, G. Liang, P. Fan, M. U. Muzaffar, B. Jabar, Z. Ge, and Z. Zheng, Realizing high thermoelectric performance via selective resonant doping in oxyselenide BiCuSeO, *Nano Res.* 16(1), 1679 (2023)
15. X. Lin, X. Dai, Z. Ye, Y. Shu, Z. Song, and X. Peng, Highly-efficient thermoelectric-driven light-emitting diodes based on colloidal quantum dots, *Nano Res.* 15(10), 9402 (2022)
16. Z. Zhu, J. Tiwari, T. Feng, Z. Shi, Y. Lou, and B. Xu, High thermoelectric properties with low thermal conductivity due to the porous structure induced by the dendritic branching in N-type PbS, *Nano Res.* 15(5), 4739 (2022)
17. S. Kawano, T. Tadano, and S. Iikubo, Effect of Halogen ions on the low thermal conductivity of cesium halide perovskite, *J. Phys. Chem. C* 125(1), 91 (2021)
18. M. Sajjad, Q. Mahmood, N. Singh, and J. A. Larsson, Ultralow lattice thermal conductivity in double perovskite Cs_2PtI_6: A promising thermoelectric material, *ACS Appl. Energy Mater.* 3(11), 11293 (2020)
19. S. Ahmad, P. Fu, S. Yu, Q. Yang, X. Liu, X. Wang, X. Wang, X. Guo, and C. Li, Dion–Jacobson phase 2D layered perovskites for solar cells with ultrahigh stability, *Joule* 3(3), 794 (2019)
20. R. Azmi, E. Ugur, A. Seitkhan, F. Aljamaan, A. S. Subbiah, J. Liu, G. T. Harrison, M. I. Nugraha, M. K. Eswaran, M. Babics, Y. Chen, F. Xu, T. G. Allen, A. Rehman, C. L. Wang, T. D. Anthopoulos, U. Schwingenschlögl, M. De Bastiani, E. Aydin, and S. De Wolf, Damp heat-stable perovskite solar cells with tailored-dimensionality 2D/3D heterojunctions, *Science* 376(6588), 73 (2022)
21. Y. Wei, B. Chen, F. Zhang, Y. Tian, X. Yang, B. Cai, and J. Zhao, Compositionally designed 2D Ruddlesden–Popper perovskites for efficient and stable solar cells, *Solar RRL* 5(4), 2000661 (2021)
22. G. Zhao, J. Xie, K. Zhou, B. Xing, X. Wang, F. Tian, X. He, and L. Zhang, High-throughput computational material screening of the cycloalkane-based two-dimensional Dion–Jacobson halide perovskites for optoelectronics, *Chin. Phys. B* 31(3), 037104 (2022)
23. P. H. Tan, L. Zhang, L. Dai, and S. Zhou, Preface to the special issue on 2D-materials-related physical properties and optoelectronic devices, *J. Semicond.* 40(6),

060101 (2019)

24. X. Yan, W. Fan, F. Cheng, H. Sun, C. Xu, L. Wang, Z. Kang, and Y. Zhang, Ion migration in hybrid perovskites: Classification, identification, and manipulation, *Nano Today* 44, 101503 (2022)
25. A. D. Christodoulides, P. Guo, L. Dai, J. M. Hoffman, X. Li, X. Zuo, D. Rosenmann, A. Brumberg, M. G. Kanatzidis, R. D. Schaller, and J. A. Malen, Signatures of coherent phonon transport in ultralow thermal conductivity two-dimensional Ruddlesden–Popper phase perovskites, *ACS Nano* 15(3), 4165 (2021)
26. C. Pipitone, S. Boldrini, A. Ferrario, G. Garcìa-Espejo, A. Guagliardi, N. Masciocchi, A. Martorana, and F. Giannici, Ultralow thermal conductivity in 1D and 2D imidazolium-based lead halide perovskites, *Appl. Phys. Lett.* 119(10), 101104 (2021)
27. S. Thakur, Z. Dai, P. Karna, N. P. Padture, and A. Giri, Tailoring the thermal conductivity of two-dimensional metal halide perovskites, *Mater. Horiz.* 9(12), 3087 (2022)
28. C. Li, H. Ma, T. Li, J. Dai, M. A. J. Rasel, A. Mattoni, A. Alatas, M. G. Thomas, Z. W. Rouse, A. Shragai, S. P. Baker, B. Ramshaw, J. P. Feser, D. B. Mitzi, and Z. Tian, Remarkably weak anisotropy in thermal conductivity of two-dimensional hybrid perovskite butylammonium lead iodide crystals, *Nano Lett.* 21(9), 3708 (2021)
29. C. Ge, M. Hu, P. Wu, Q. Tan, Z. Chen, Y. Wang, J. Shi, and J. Feng, Ultralow thermal conductivity and ultrahigh thermal expansion of single-crystal organic–inorganic hybrid perovskite $CH_3NH_3PbX_3$ (X = Cl, Br, I), *J. Phys. Chem. C* 122(28), 15973 (2018)
30. G. A. Elbaz, W. L. Ong, E. A. Doud, P. Kim, D. W. Paley, X. Roy, and J. A. Malen, Phonon speed, not scattering, differentiates thermal transport in lead halide perovskites, *Nano Lett.* 17(9), 5734 (2017)
31. P. Acharyya, T. Ghosh, K. Pal, K. Kundu, K. Singh Rana, J. Pandey, A. Soni, U. V. Waghmare, and K. Biswas, Intrinsically ultralow thermal conductivity in Ruddlesden–Popper 2D perovskite $Cs_2PbI_2Cl_2$: Localized anharmonic vibrations and dynamic octahedral distortions, *J. Am. Chem. Soc.* 142(36), 15595 (2020)
32. J. Tang, C. Qin, H. Yu, Z. Zeng, L. Cheng, B. Ge, Y. Chen, W. Li, and Y. Pei, Ultralow lattice thermal conductivity enables high thermoelectric performance in $BaAg_2Te_2$ alloys, *Mater. Today Phys.* 22, 100591 (2022)
33. T. Parashchuk, R. Knura, O. Cherniushok, and K. T. Wojciechowski, Ultralow lattice thermal conductivity and improved thermoelectric performance in Cl-doped $Bi_2Te_{3-x}Se_x$ alloys, *ACS Appl. Mater. Interfaces* 14(29), 33567 (2022)
34. Y. Q. Cao, T. J. Zhu, and X. B. Zhao, Low thermal conductivity and improved figure of merit in fine-grained binary PbTe thermoelectric alloys, *J. Phys. D Appl. Phys.* 42(1), 015406 (2009)
35. X. Wang, M. Faizan, K. Zhou, H. Zou, Q. Xu, Y. Fu, and L. Zhang, Exploration of B-site alloying in partially reducing Pb toxicity and regulating thermodynamic stability and electronic properties of halide perovskites, *Sci. China Phys. Mech. Astron.* 66(3), 237311 (2023)
36. T. J. Slade, T. P. Bailey, J. A. Grovogui, X. Hua, X. Zhang, J. J. Kuo, I. Hadar, G. J. Snyder, C. Wolverton, V. P. Dravid, C. Uher, and M. G. Kanatzidis, High thermoelectric performance in PbSe–$NaSbSe_2$ alloys from valence band convergence and low thermal conductivity, *Adv. Energy Mater.* 9(30), 1901377 (2019)
37. Y. Zheng, C. Liu, L. Miao, C. Li, R. Huang, J. Gao, X. Wang, J. Chen, Y. Zhou, and E. Nishibori, Extraordinary thermoelectric performance in MgAgSb alloy with ultralow thermal conductivity, *Nano Energy* 59, 311 (2019)
38. G. Kresse and J. Furthmüller, Efficiency of *ab-initio* total energy calculations for metals and semiconductors using a plane-wave basis set, *Comput. Mater. Sci.* 6(1), 15 (1996)
39. G. Kresse and D. Joubert, From ultrasoft pseudopotentials to the projector augmented-wave method, *Phys. Rev. B* 59(3), 1758 (1999)
40. C. Braga and K. P. Travis, A configurational temperature Nosé–Hoover thermostat, *J. Chem. Phys.* 123(13), 134101 (2005)
41. O. Hellman, P. Steneteg, I. A. Abrikosov, and S. I. Simak, Temperature dependent effective potential method for accurate free energy calculations of solids, *Phys. Rev. B* 87(10), 104111 (2013)
42. O. Hellman, I. A. Abrikosov, and S. I. Simak, Lattice dynamics of anharmonic solids from first principles, *Phys. Rev. B* 84(18), 180301 (2011)
43. W. Li, J. Carrete, N. A. Katcho, and N. Mingo, ShengBTE: A solver of the Boltzmann transport equation for phonons, *Comput. Phys. Commun.* 185(6), 1747 (2014)
44. D. A. Broido, M. Malorny, G. Birner, N. Mingo, and D. A. Stewart, Intrinsic lattice thermal conductivity of semiconductors from first principles, *Appl. Phys. Lett.* 91(23), 231922 (2007)
45. A. Ward, D. A. Broido, D. A. Stewart, and G. Deinzer, *Ab initio* theory of the lattice thermal conductivity in diamond, *Phys. Rev. B* 80(12), 125203 (2009)
46. W. Li, L. Lindsay, D. A. Broido, D. A. Stewart, and N. Mingo, Thermal conductivity of bulk and nanowire $Mg_2Si_xSn_{1-x}$ alloys from first principles, *Phys. Rev. B* 86(17), 174307 (2012)
47. R. D. Shannon, Revised effective ionic radii and systematic studies of interatomic distances in halides and chalcogenides, *Acta Crystallogr. A* 32(5), 751 (1976)
48. W. Pu, W. Xiao, J. Wang, X. Li, and L. Wang, Screening of perovskite materials for solar cell applications by first-principles calculations, *Mater. Des.* 198, 109387 (2021)
49. I. L. Ivanov, A. S. Steparuk, M. S. Bolyachkina, D. S. Tsvetkov, A. P. Safronov, and A. Yu. Zuev, Thermodynamics of formation of hybrid perovskite-type methylammonium lead halides, *J. Chem. Thermodyn.* 116, 253 (2018)
50. K. Komiya, N. Morisaku, R. Rong, Y. Takahashi, Y. Shinzato, H. Yukawa, and M. Morinaga, Synthesis and decomposition of perovskite-type hydrides, $MMgH_3$ (M= Na, K, Rb), *J. Alloys Compd.* 453(1–2), 157 (2008)
51. A. Gold-Parker, P. M. Gehring, J. M. Skelton, I. C. Smith, D. Parshall, J. M. Frost, H. I. Karunadasa, A. Walsh, and M. F. Toney, Acoustic phonon lifetimes limit thermal transport in methylammonium lead iodide, *Proc. Natl. Acad. Sci. USA* 115(47), 11905 (2018)